Computers and Geotechnics 45 (2012) 19–33

Contents lists available at SciVerse ScienceDirect

Computers and Geotechnics

journal homepage: www.elsevier.com/locate/compgeo

A three-dimensional numerical investigation of the fracture of rock specimens containing a pre-existing surface flaw

Z.Z. Liang [a,b,*], H. Xing [b], S.Y. Wang [c], D.J. Williams [d], C.A. Tang [e]

[a] State Key Laboratory of Coastal and Offshore Engineering, Dalian University of Technology, Dalian 116024, China
[b] Earth System Science Computational Centre, The University of Queensland, Brisbane, QLD 4072, Australia
[c] Centre for Geotechnical and Materials Modelling, Department of Civil, Surveying and Environmental Engineering, The University of Newcastle, Callaghan, NSW 2308, Australia
[d] Golder Geomechanics Centre, School of Civil Engineering, The University of Queensland, Brisbane, QLD 4072, Australia
[e] School of Civil Engineering, Dalian University of Technology, Dalian 116024, China

ARTICLE INFO

Article history:
Received 1 April 2011
Received in revised form 10 February 2012
Accepted 30 April 2012
Available online 31 May 2012

Keywords:
Surface flaw
Heterogeneity
Mode III fracture
Three-dimensional model
Finite element
Wing cracks

ABSTRACT

Three-dimensional surface crack initiation and propagation in two kinds of heterogeneous rocks were numerically investigated via parallel finite element analysis using a supercomputer. Numerically simulated rock specimens containing a pre-existing flaw were subjected to uniaxial compression until failure. The initiation and propagation of wing cracks, anti-wing cracks, and shell-like cracks were reproduced by numerical simulations. The numerically simulated results demonstrate that the further propagation of wing cracks and shell-like cracks stop due to their wrapping (curving) behavior in three-dimensional spaces, even if the applied loads continue to increase. Furthermore, rock heterogeneity could significantly influence crack propagation patterns and the peak uniaxial compressive strengths of rock specimens. Moreover, anti-wing cracks only appeared in relatively heterogeneous rocks, and the peak uniaxial compressive strengths of the specimens were observed to depend on the inclination of the pre-existing flaw. Finally, the mechanism of surface crack propagation is discussed in the context of numerically simulated anti-plane loading tests, wherein it was identified that Mode III loading (anti-plane loading) does not lead to Mode III fracture in rocks due to their high ratio of uniaxial compressive strength to tensile strength. This finding could explain the lateral growth of an existing flaw in its own plane, which is a phenomenon that has not been observed in laboratory experiments.

© 2012 Elsevier Ltd. All rights reserved.

1. Introduction

The Earth's crust consists of rocks, and fractures normally exist in all rocks. These fractures vary at different scales, ranging from microcracks to all kinds of macrojoints to continental faults. The failure of heterogeneous rocks under compression is preceded by the initiation and accumulation of new cracks and the propagation of existing cracks [1,2]. The deformations and strengths of rock masses depend on the spacing, direction and scale of the joints (fractures) that are distributed throughout them. Therefore, an understanding of the mechanisms of crack initiation and propagation processes in rocks is crucial for the reliable performance of many geotechnical structures, such as tunnels, slopes and dams [3].

In recent decades, many laboratory experimental investigations have studied crack initiation and propagation in rocks. Dyskin and co-authors conducted a series of uniaxial compression tests on transparent models (such as resin, polymethyl methacrylate (PMMA), and borosilicate glass) that contained internal three-dimensional (3D) flaws [4,5]. They observed that wing cracks initiated and propagated only to approximately the size of the initial flaw and then stopped. This type of crack did not further propagate even with an additional applied loading. In Dyskin's opinion, this cracking behavior can be explained by the wrapping (curving) of emerging wings around the initial crack [4,5]. Teng et al. also investigated frictional cracking from a 3D surface crack in various materials, including PMMA, glass and marble [6]. Their experimental results were similar to those of Dyskin's, in which further loading was observed to not result in further wing crack propagation [7]. In view of these observations, Sahouryeh and Dyskin experimentally investigated 3D crack growth under biaxial compression [8]. They found that the growth behavior of an internal crack under biaxial compression markedly differed from that observed under uniaxial compression. The presence of the intermediate principal compressive stress prevented the curling (wrapping) behavior of

* Corresponding author at: State Key Laboratory of Coastal and Offshore Engineering, Dalian University of Technology, Dalian 116024, China.
E-mail addresses: Z.Z.Liang@163.com (Z.Z. Liang), h.xing@uq.edu.au (H. Xing), Shanyong.Wang@newcastle.edu.au (S.Y. Wang), d.williams@uq.edu.au (D.J. Williams), tca@mail.neu.edu.cn (C.A. Tang).

0266-352X/$ - see front matter © 2012 Elsevier Ltd. All rights reserved.
http://dx.doi.org/10.1016/j.compgeo.2012.04.011

wings, thereby enabling an extensive growth of crack branches, which ultimately resulted in splitting failure.

Recently, several experiments concerning 3D fault growth have been investigated at the Rock Mechanics Laboratory at The Hong Kong Polytechnic University. The samples that were investigated in those experiments included a variety of real rocks, PMMA, resin, cement, and gypsum samples. All samples contained a prefabricated 3D surface flaw [3,9–12]. According to their experiments, both tensile cracks and petal cracks can initiate from flaw tips in both PMMA and marble specimens, and shell-like cracks can initiate from the flaw tips of both PMMA and marble specimens in some cases. Moreover, anti-wing cracks (opposite to wing cracks) were induced at a certain distance away from the flaw tips in the compressive stress zone in gabbro specimens [9]. Liu et al. conducted a series of experimental tests to study the 3D propagation processes of a single surface flaw under the conditions of biaxial compression [13]. In their experimental tests, a high-density, multi-channel digital strain gauge (MCDSG), a digital speckle correlation method (DSCM) based on white-light image analysis, and a 3D acoustic emission (AE) location system were used. They also observed shell-shaped fracturing on the sample surface in the last stage of the 3D propagation process of surface flaws [13].

Typically, an initial crack can grow in the lateral direction due to Mode III conditions that exist at the lateral parts of the initial crack contour [14]. Mode III cracks are known to grow in their own plane by producing an array of microcracks in brittle materials [15]; however, the actual lateral propagation of the initial crack was not observed in either of the experiments of Adams and Sines [16] and Cannon et al. [17]. Even in specifically designed experiments that permit crack growth, such as those performed by Dyskin et al. [4] on large transparent blocks of polyester casting resin and others on PMMA blocks, the observed crack growth was only moderate. Dyskin thought this was the major difference between two-dimensional (2D) and three-dimensional crack propagation mechanisms in uniaxial compression [4].

In terms of rock experiments, due to the non-transparency of rock, it is difficult to trace the initiation and propagation of fractures within the rock. Although some new techniques are utilized to measure and observe the fracturing process [12,13], it is too expensive to conduct a large number of such experiments. In contrast, numerical methods provide an alternate way to study crack initiation, propagation and coalescence in rock and/or rock-like materials. Many numerical methods have been applied to investigate the fracturing of cracks in rocks [18–32].

The FEM remains a main numerical tool in rock mechanics problems because of its maturity and advantages in handling rock heterogeneity and non-linearity, and the availability of many well-verified commercial codes. The traditional FEM is handicapped by the requirement of continuous re-meshing with fracture growth, and conformable fracture path and small element size. A special class of FEM, often called 'enriched FEM' or 'extended FEM (XFEM)', has been especially developed for fracture analysis with minimal or no re-meshing. The XFEM with jump functions and crack tip functions has improved the FEM's capacity in fracture analysis. Rozycki et al. applied XFEM to simulate the dynamic problem [23]. Colombo et al. proposed a fast and robust level set update to simulate the complex 3D crack propagations efficiently simulated in an X-FEM model [25]. The XFEM may become a promising subject for further research and development for the problems of fractured rocks.

The BEM, requires discretization at the boundary of the solution domains only, thus reducing the problem dimensions by one and greatly simplifying the input requirements. The main advantage of the BEM is the reduction of the computational model dimension by one, with much simpler mesh generation and therefore input data preparation, compared with full domain discretization methods such as the FEM. Chen et al. investigated the deformability, tensile strength and fracturing of anisotropic rocks by Brazilian test by using a new formulation of the BEM to determine the stress intensity factors (SIFs) and the fracture toughness of anisotropic rocks [18]. Shen et al. investigated the mechanism of fracture coalescence by uniaxial compression of gypsum samples with two open or closed cracks by using a modified G-criterion and displacement discontinuity method (DDM), and they found that coalescence could be caused by tensile failure, shear failure or mixed tensile and shear failure, and Mode II failure was the key reason for the coalescence between two non-overlapping cracks [19,20]. However, in general, the BEM is not as efficient as the FEM in dealing with material heterogeneity, because it cannot have as many sub-domains as elements in the FEM. It is also not as efficient as the FEM in simulating non-linear material behavior, such as plasticity and damage evolution processes.

EPCA model is a useful method for simulating the rock fracturing process using simple rules. Feng et al. simulated the failure process of heterogeneous rocks successfully by using an elastoplastic cellular automation [21,22].

Among all of these numerical methods, the FEM is perhaps the most widely applied numerical method in rock mechanics problems today because its flexibility in handling material heterogeneity, non-linearity and boundary conditions, with many well developed and verified commercial codes with large capacities in terms of computing power, material complexity and user friendliness.

Tang et al. developed and applied the finite element code of rock failure process analysis (RFPA^{2D}) to investigate fracture initiation, propagation and coalescence from a pre-existing flaw in rock-like materials [26]. The numerically simulated results agreed with the experimental results of Wong et al. [34]; however, as far as the numerical simulations of 3D fractures from surface flaws are concerned, little information has been reported in the literature.

In addition, due to the heterogeneity of rock and the complicated boundary conditions therein, it is difficult to use fracture mechanics to establish an analytical model to investigate the initiation, propagation and coalescence of 3D cracks [13,35]. In this study, RFPA^{3D} numerical analysis, which is an extension of RFPA^{2D}, was applied to investigate the 3D fracturing processes of rock samples with single pre-existing flaws at different dip angles. Two kinds of rock heterogeneities and different pre-existing flaw dip angles were considered. In addition, anti-plane loading tests were also numerically simulated to investigate the fracture process of the surface flaws.

2. Brief description of RFPA^{3D}

When a heterogeneous material is concerned, the disorder of microstructures in rock should be implemented in a numerical model. To simulate the random microstructures in rock, rock heterogeneity can be well characterized using statistical approaches [26,27]. In RFPA^{3D}, it is assumed that the numerical specimens consist of the elements with the same shape and size and that there is no geometric priority in any orientation in the specimen [28]. Disorder can be obtained by randomly distributing the mechanical properties of elements. The statistical distribution of elemental mechanical parameters can be described by the Weibull distribution function [36], even distribution function, or normal distribution function [27,28]. These elemental mechanical parameters include the uniaxial compressive strength, elastic modulus, Poisson ratio and weight. Only the Weibull distribution function was used in the present paper, as is detailed below [36]:

$$W(x) = \frac{m}{x_0}\left(\frac{x}{x_0}\right)^{m-1} \exp\left[-\left(\frac{x}{x_0}\right)^{m}\right] \quad (1)$$

where m defines the shape of the Weibull distribution function, and it can be referred to as the homogeneity index [26], x is the mechanical

parameter of one element, and x_0 is the even value of the parameter of all the elements. According to the Weibull distribution [36], a larger m value indicates that more elements have mechanical properties that have been approximated to the mean value, which describes a more homogeneous rock specimen. Fig. 1a depicts the elastic modulus distribution in two specimens with heterogeneity indices of 5.0 and 50.0. In this figure, the mean value for all of the elements is 2000 MPa; however, for specimens with heterogeneity indices of 5.0 and 50.0, the maximal values for all of the elements were 5.257×10^4 MPa and 2.079×10^4 MPa, respectively, and the minimal values for all of the elements were 6.326×10^2 MPa and 1.742×10^4 MPa, respectively, as shown in Fig. 1b. For the specimen with m = 50.0, the elements therein had a greater probability to reach the mean elastic modulus value.

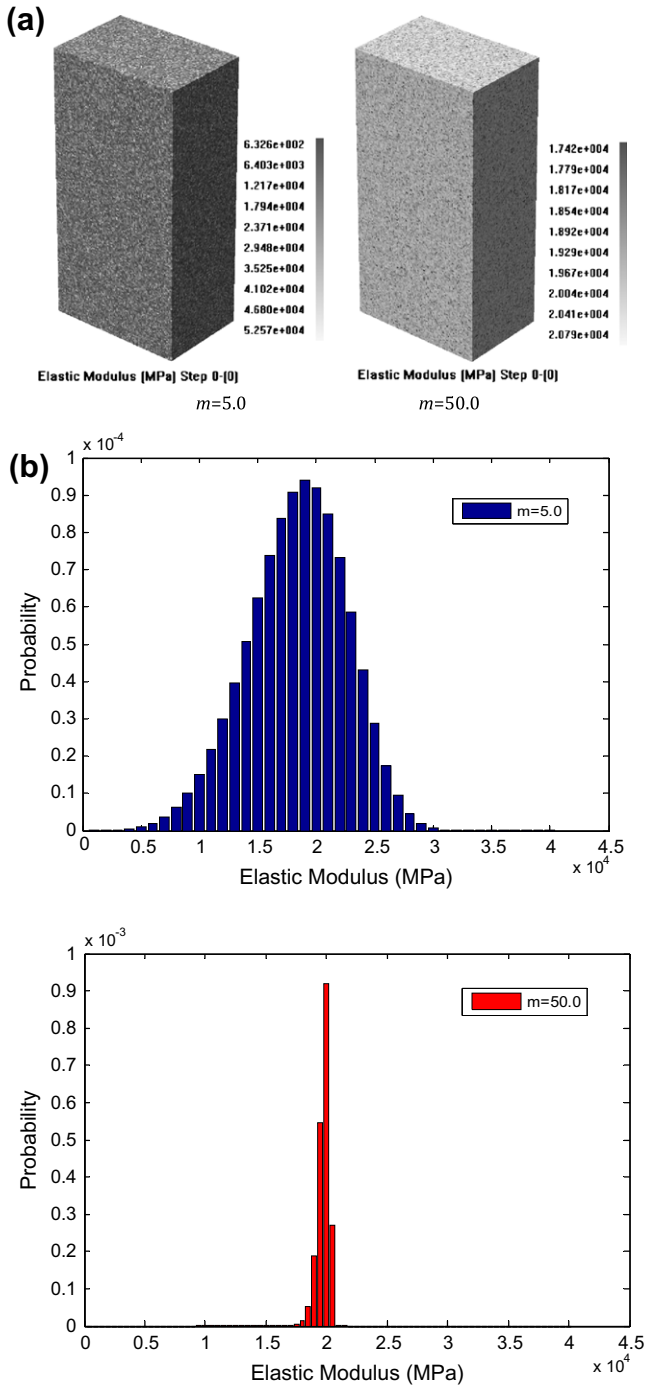

Fig. 1. (a) Two specimens with different heterogeneity indices. Heterogeneity is introduced into the numerical specimens by following a Weibull distribution function. The grey color represents the mechanical parameter value relatively. (b) Distribution probability of the elastic modulus for the two specimens with different heterogeneity indices. The mean value of the elastic modulus for these two model is 20,000 MPa.

In RFPA code, each element has an elastic–brittle constitutive law during the failure process [28,29]. The constitutive relation for an element under uniaxial tensile stress is illustrated in Fig. 2a. Before the stress of the element satisfies the strength criterion, the elastic modulus is a constant with the same value as before loading. When the stress increases to a value leading to the failure of the element, in elastic damage mechanics the elastic modulus of the element may degrade gradually as damage progresses. The elastic modulus of the damaged element is defined as follows:

$$E = (1 - D)E_0 \tag{2}$$

where D represents the damage variable, and E and E_0 are the elastic modulus of the damaged and undamaged elements, respectively. It must be noted that the element and its damage are assumed to be isotropic, and therefore E, E_0 and D are all scalar.

If the element is subjected to uniaxial tensile stress, before the tensile stress (the minimal principal stress) of the element reaches its tensile strength σ_t, the element keeps linear elastic. When $\sigma_3 > \sigma_t$, the element fails and the elastic modulus changes to a small value and its strength falls to σ_{rt}, which we can call it residual tensile strength. When the tensile strain increases to a more large value ε_{ut}, the element loses his capability of loading. The evolution of damage variable D can be summarized as following:

$$D = \begin{cases} 0 & (\bar{\varepsilon} > \varepsilon_{t0}) \\ 1 - \frac{\sigma_{rt}}{\varepsilon E_0} & (\varepsilon_{t0} \leqslant \bar{\varepsilon} \leqslant \varepsilon_{ut}) \\ 1 & (\bar{\varepsilon} \leqslant \varepsilon_{ut}) \end{cases} \tag{3}$$

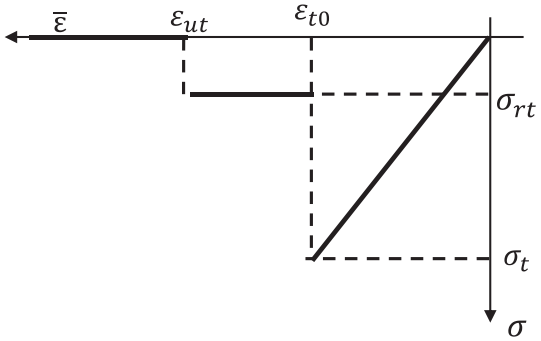

(a) The constitutive law of the element in tensile failure.

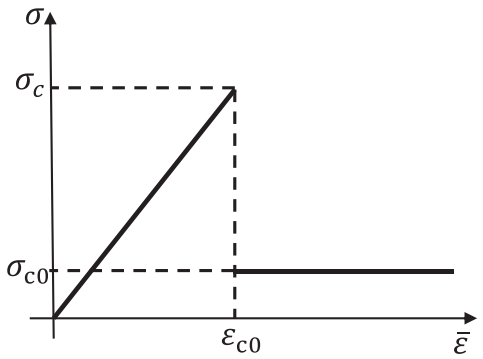

(b) The constitutive law for the element in shear failure

Fig. 2. The constitutive law for the element in two different failure modes.

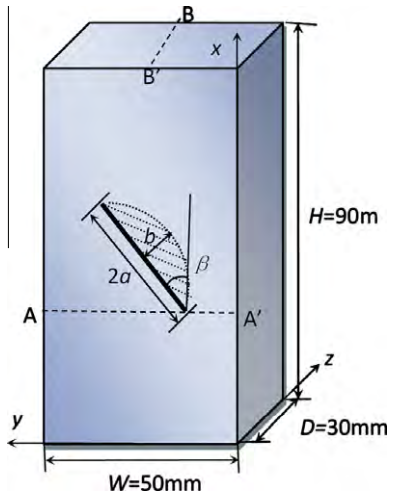

Fig. 3. Layout of the numerical specimens with a single pre-existing flaw.

where σ_{rt} is the residual strength of the element, and $\sigma_{rt} = -\lambda|\sigma_t|$. ε_{t0} is the tensile strain at the point of failure. ε_{ut} is the ultimate tensile strain and can be described as $\varepsilon_{ut} = \eta\varepsilon_{t0}$. η is the ultimate tensile strain coefficient and λ is coefficient of residual tensile strength. $\bar{\varepsilon}$ is equivalent principal strain of the element, ε_{to} is the strain at the elastic limit, or threshold strain, and ε_{tu} is the ultimate tensile strain of the element at which the element would be completely damaged. The equivalent principal strain $\bar{\varepsilon}$ is defined as [29,30]:

$$\bar{\varepsilon} = \sqrt{\langle\varepsilon_1\rangle^2 + \langle\varepsilon_2\rangle^2 + \langle\varepsilon_3\rangle^2} \tag{4}$$

where ε_1, ε_2 and ε_3 are three principal strains and $\langle\ \rangle$ is a function defined as follows:

$$\langle x\rangle = \begin{cases} x & x \geqslant 0 \\ 0 & x < 0 \end{cases} \tag{5}$$

When the equivalent strain of an element decreases to be smaller than the ultimate tensile strain, the damaged elastic modulus is zero, which would make the system of equations ill-conditioned. In order to keep the continuum of the numerical model physically, the element is not removed from the model and a relatively small number, i.e. 1.0×10^{-6} is specified for the elastic modulus for this consideration. Shear failure is also assumed to exist when the element is under compressive and shear stress. The constitutive law for the elements in microscales under compressive or shear stress is shown in Fig. 2b. In shear failure mode, the damage variable D can be described as follows:

$$D = \begin{cases} 0 & \bar{\varepsilon} < \varepsilon_{c0} \\ 1 - \frac{\sigma_{rc}}{E_0\bar{\varepsilon}} & \bar{\varepsilon} \geqslant \varepsilon_{c0} \end{cases} \tag{6}$$

where σ_{rc} is the peak strength of the element subjected to uniaxial compression and σ_{c0} is the compressive stress at the point of shear failure (Fig. 2b).

Before the stress of the element satisfies a certain strength criterion, the elastic modulus is constant with the same value. When the stress of the element satisfies the strength criterion, the elastic modulus of the element may damage [28,29]. If the elemental stress state satisfies both the tensile failure criterion and shear failure criterion, the tensile failure mode takes the higher priority. When the tensile stress increases to a larger value, which we call the ultimate tensile strength, the element loses its loading capability. Similarly, the element maintains a linear elasticity before the uniaxial compressive stress reaches the uniaxial compressive strength. If the elemental stress meets the shear failure criterion, the element will damage [28,36–38].

The mechanical parameters of a macroscopic specimen for a specific rock specimen can be obtained from laboratory experiments; however, it is impossible to directly measure the parameters of such failed elements. For the Weibull distribution, a parametric study can be performed to obtain the relationships between the macroscopic parameters (compressive strength, σ_c, and elastic modulus, E_0) of the specimen and the seed parameters (mean value of compressive strength, $\bar{\sigma}_c$, and elastic modulus $\overline{E_0}$) of the mesoscopic elements by using the linear least squares technique.

$$\bar{\sigma}_c = [a_1 \ln(m) + b_1]\sigma_c \tag{7}$$

$$\overline{E_0} = [a_2 \ln(m) + b_2]E_0 \tag{8}$$

The uniaxial compressive strength and elastic modulus that corresponds to a specific rock can be obtained from laboratory experiments. Because rock is a geotechnical material that has dramatically different tensile and compressive strengths, the coefficient β can be used to define the ratio of the compressive strength to the tensile strength of a numerically modeled rock. The shape parameter, m, in a Weibull distribution function, can be obtained as a matter of experience from experimental and numerical tests. More detailed descriptions can be found in other publications [26–33].

It should be noted that even under uniaxial compression, both tensile damage and shear damage may occur in the elements due to a complicated stress state that is caused by the heterogeneity of rock and the pre-existing flaw in the rock specimen. In 3D studies, the traditional Mohr–Coulomb strength criterion or Hoek–Brown strength criterion is not valid when the effect of intermediate principal stress is considered. Higher strength values were observed under the condition of plane strain, which was due to the strengthening effect of the intermediate principal stress [39–42]. Therefore, the Drucker–Prager strength criterion and unified strength criterion proposed by Yu [42], which consider all three of the principal stresses, are adopted in RFPA^{3D}. A simplified unified strength criterion, which is referred to as the twins shear failure criterion, can be expressed as follows [42]:

$$\begin{aligned} F &= \sigma_1 - \tfrac{\alpha}{2}(\sigma_2 + \sigma_3) = \sigma_t \quad \sigma_2 \leqslant \tfrac{\sigma_1 + \alpha\sigma_3}{1+\alpha} \\ F &= \tfrac{1}{2}(\sigma_2 + \sigma_3) - \alpha\sigma_3 = \sigma_t \quad \sigma_2 > \tfrac{\sigma_1 + \alpha\sigma_3}{1+\alpha} \end{aligned} \tag{9}$$

where σ_1, σ_2 and σ_3 are the maximal, intermediate and minimal principal stresses, respectively, and α is the influence coefficient of the intermediate principal stress.

The tensile failure criterion can be expressed as follows:

$$\sigma_3 \leqslant -|\sigma_t| \tag{10}$$

where σ_t is the tensile strength of the rock.

To perform finite element analysis, the parameters of the numerical model are specified together with the initial boundary conditions. A finite element analyzer is used to calculate the stress and strain distributions in the finite element network. The calculated stresses are substituted into the strength criterion to check whether elemental damage occurs or not. If the strength criterion is not satisfied, the external loading or displacement loading is further increased. Otherwise, the element is damaged and becomes weak according to the rules specified by the mesoscopic elemental mechanical model for elastic damage [29], which results in a new perturbation. The stress and deformation distributions throughout the model are then instantaneously adjusted after such rupture so as to reach the equilibrium state. Due to the new stress disturbances, the stresses of some elements may satisfy the critical value, causing further ruptures. This process is repeated until no damaged

elements are found. The external load is then increased further. In this way, the system develops a macroscopic fracture such that the propagation of fractures can be simulated [28,29].

In addition, an acoustic emission (AE) technique is used to monitor the cracking processes taking place in some portions of rock mass. In RFPA^{3D}, the failure (or damage) of every element is assumed to be the source of an acoustic event because the failed element must release its elastic energy stored during the deformation. Therefore, by recording the number of damaged elements and the associated amount of energy release, RFPA^{3D} is capable of simulating AE activities, including the AE event rate, magnitude and location.

RFPA^{3D} includes the following three modules: the pre- and post-processing module, FEM module and failure analysis module. The pre- and post-processing module is implemented by the Visual C++ language, whereas the other two modules are developed using the FORTRAN 95 language and message passing interface (MPI), which can run on both PC and parallel computers.

3. Numerical model setup

Ten specimens were prepared to numerically investigate 3D crack behaviors under uniaxial compressive loading (from case 1–10), as detailed in Table 1. Two groups of materials with different heterogeneities (i.e., $m = 5.0$ and $m = 50.0$) were used. The higher homogeneity index of a specimen indicates that it has relatively homogenous features such that the macromechanical parameters are close to the specified mean values [19–21]. The specimen with $m = 5.0$ represents a heterogeneous rock with a fine-grained texture, whereas the specimen with the higher homogeneity index of $m = 50.0$ represents relatively more homogeneous rock, such as glass or PMMA. To simplify the analysis, only two different homogeneity indices (m) were investigated. The effect of different homogeneity indices (m) on the fracturing mechanisms of pre-existing flaws in rock will be discussed in a later manuscript.

To investigate the effect of dip angle on fracture behavior, each group was selected using the following pre-existing flaw dip angles: 15°, 30°, 45°, 60° and 75° (Table 1). These five specimens in each group have the same mechanical parameters, including homogeneity index, elastic modulus, peak strength, and also have the same geometric size (90 mm × 50 mm × 30 mm). The initial mean values of the uniaxial compressive strength, elastic modulus and Poisson ratio for all of the elements in the aforementioned specimens were 100 MPa, 20,000 MPa and 0.25, respectively.

A semi-elliptic flaw was embedded at the center of each specimen, as shown in Fig. 2. The flaw surface is perpendicular to the *xoy* surface, and the major axis lies on the *xoy* surface. The dip angle of the major axis relative to the *x*-axis (compressive loading stress direction) was varied from 15° to 75° at intervals of 15°. Half of the major axial diameter (a) was set to 12 mm, half of the minor axial diameter (b) was set to 8 mm, and the thickness of the flaw was set to 1 mm. To simulate open cracks in rocks, the surfaces of the prepared flaws were not allowed to touch one another and there was assumed to be zero friction transfer. Actually, the elements in the surface flaw were not removed but, instead, replaced by very soft elements with very small elastic module that could be ignored. The dimensions for all of the specimens were the same. To reduce the boundary effect [3], the depth was set to be 30 mm, which is more than three times the half minor axial diameter. The height and width of the specimens were 90 mm and 50 mm, respectively. The specimens were meshed into 180 × 100 × 60 = 1,080,000 finite elements. A displacement control of 0.002 mm per step was axially applied on the top and bottom of the specimen.

Table 1
Different flaw dip angles and two kinds of homogeneity indices of rock are considered.

	Case no.	Flaw dip angle of (°)	Homogeneity index (m)
Group 1	1	15	5.0
	2	30	5.0
	3	45	5.0
	4	60	5.0
	5	75	5.0
Group 2	6	15	50.0
	7	30	50.0
	8	45	50.0
	9	60	50.0
	10	75	50.0

According to a study by Wong et al. [11], pre-existing fractures can be referred to as flaws, whereas initiated fractures can be referred to as cracks. Shell-like cracks that initiated from the inner contour of the existing flaw along the loading direction have often been referred to as wing cracks in many investigations. In this present study, these cracks were referred to as shell-like cracks so as to distinguish them from wing cracks in the 2D study.

4. Numerically simulated results

Based on the numerically simulated results, the complete failure process of the specimens that were subjected to uniaxial compression can be divided into four stages: the elastic deformation stage before crack initiation, the crack initiation stage, the crack propagation stage and the final failure stage. The elastic deformation stage is normal and, thus, only the simulation results of the latter three stages are described below.

4.1. Crack initiation

Fig. 4a–e depicts the crack initiation patterns for the specimens that contained pre-existing flaws with different dip angles. When the orientation angle was smaller than 60°, wing cracks were observed (Fig. 4a–d), whereas anti-wing cracks were observed in the specimen with a dip angle of 75° (Fig. 4e). All of the wing cracks were observed to have initiated at the tips of the pre-existing flaws. The initial wing cracks propagated parallel to the vertical loading direction for the specimens with the flaw dip angles of 15° and 30°, whereas, in the specimens with flaw dip angles that varied from 30° to 45° to 60°, the initial wing cracks were observed to propagate along the direction perpendicular to the surfaces of the prepared flaws; however, with increasing load, the wing cracks in the specimens with the flaw dip angles that varied from 30° to 45° to 60° changed their direction from perpendicular to the flaw surface to parallel to the maximal compressive stress.

Anti-wing cracks, which initiate at the tips of flaws and propagate along the direction that is opposite to the wing crack, were only observed in the specimen with a flaw dip angle of 75°. In addition to the anti-wing cracks, due to the tensile stress, several vertical cracks were observed to have initiated perpendicular to the surface of the prepared flaw (Fig. 4e). These vertical cracks were observed to propagate more slowly than anti-wing cracks when subjected to further uniaxial compressive loads, which indicates that in the early stages of crack initiation, anti-wing crack initiation depends on the dip angle of the prepared flaw. In the early studies of Wong et al., anti-wing cracks were commonly referred to as secondary cracks and were thought to be induced by the extensions of petal cracks [3].

Fig. 4a′–e′ demonstrate the crack initiation processes in the more homogeneous specimens ($m = 50.0$). In this group, wing cracks were only observed toward the direction of the loading stress for the specimens with flaw dip angles of greater than 15°

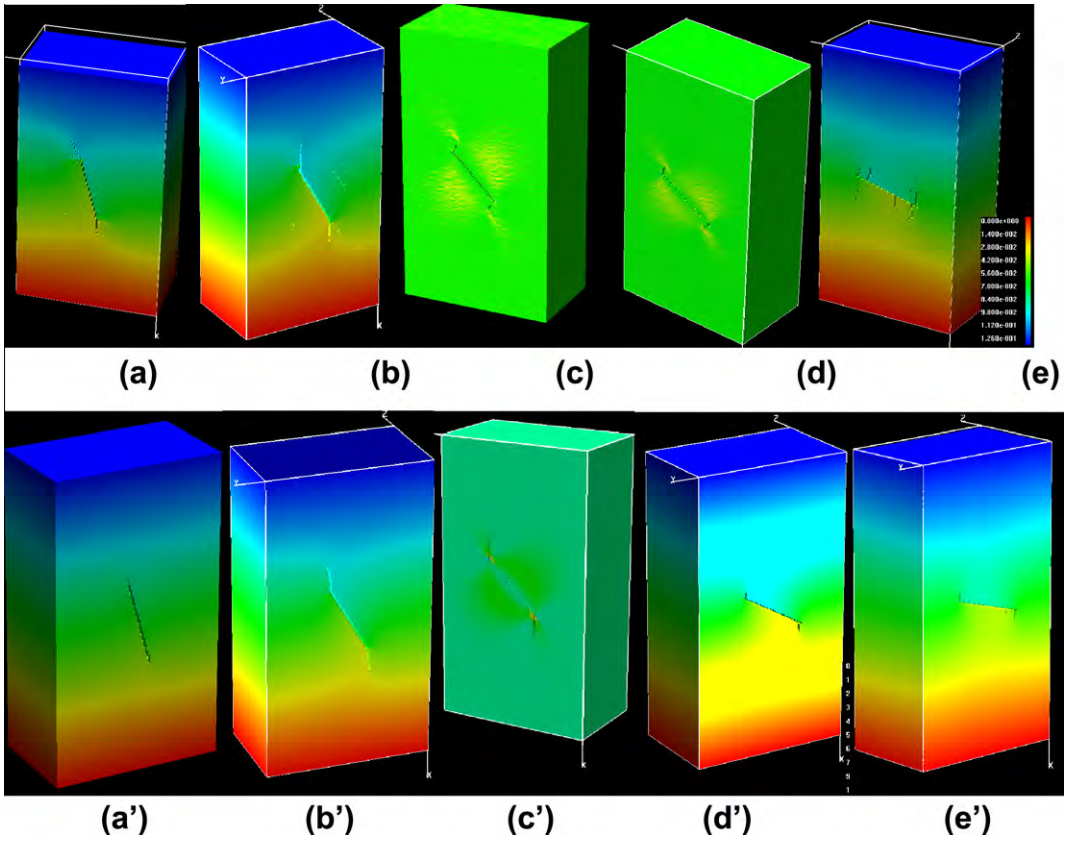

Fig. 4. Crack initiation in the specimens containing a pre-existing flaw with different dip angle of 15°, 30°, 45°, 60°and 75°. The first row (a–e) is for the relatively heterogeneous specimens (m = 5.0), and the second row (a′–e′) is for the relatively more homogeneous specimens (m = 50.0).

(Fig. 4b′–e′). Unlike the heterogeneous rock specimens, anti-wing cracks did not appear in the specimen with the flaw dip angle of 75° (Fig. 4e′). For the specimen with the flaw dip angle of 15°, new cracks were observed to have initiated at the tips of the flaw along the direction of the surface of the pre-existing flaw. In addition, in homogeneous rocks (m = 50), newly initiating wing cracks developed parallel to the loading stress (Fig. 4c′–d′), whereas in relatively heterogeneous rocks (m = 5), wing cracks were observed to have initiated perpendicular to the surfaces of the prepared flaws (Fig. 4c and d). These data indicate that the homogeneity index of rock can influence the initiation of anti-wing cracks and wing cracks.

Fig. 5 demonstrates the required stress for crack initiation versus flaw dip angle in the investigated specimens (m = 5). From Fig. 5, the required stress for crack initiation gently decreased with a low slope when the dip angle was increased from 15° to 45°. In comparison, when the dip angle was increased from 45° to 75°, the required stress for crack initiation decreased with at high slope, which indicates the existence of a transition of crack initiation from wing cracking to anti-wing cracking. That is, the stress that is required for anti-wing cracking is smaller than that for wing cracking, and a dip angle of 45° is probably the inflexion. The numerically simulated results for the effect of pre-existing flaw dip angle on crack initiation agree with the experimental results of Guo et al. [12], i.e., the stress for crack initiation also decreases when the flaw angle increases from 30° to 75°.

Fig. 6 depicts the acoustic emission counts for cases 3 and 5 before failure. At the beginning of the loading stage in case 3, the specimen underwent an elastic deformation, and no AEs were observed throughout the entire specimen until the axial displacement was increased to 0.006 mm. Beginning on the third step, a few AEs (or damaged elements) that scattered throughout the specimen were detected. Stress was observed to concentrate around the edge of the flaw, including the two tips of the flaw where wing or anti-wing cracks eventually appeared. In 2D modeling, the stress concentration around the inner edge of the flaw cannot be analyzed. When the stress was increased to 45.7% of the peak loading and the strain increased to 0.1% of the peak compressive strain, wing cracks began to initiate perpendicular to the surface of the prepared flaw. This critical point can also be determined from the AEs depicted in Fig. 6. Beginning at step 21, the AE rate suddenly increased due to the initiation of wing cracks and shell-like cracks inside of the investigated specimen. AE events appeared later in case 5 than case 3. No AEs were observed until step 2; however, a sharp increase in AEs occurred during step 25

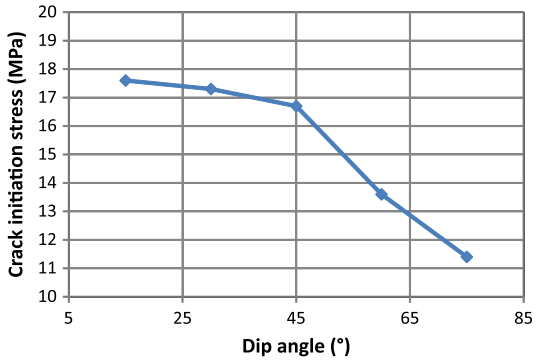

Fig. 5. The stress required for crack initiation for the specimens (m = 5.0) versus the flaw dip angles.

due to the initiation of anti-wing cracks. As shown in Fig. 4e, there were several vertical cracks that were perpendicular to the prepared flaw and parallel to the anti-wing cracks. The initiations of these cracks contributed to increases in the frequency of AEs in a stepwise manner.

4.2. Crack propagation

Fig. 7a–e depict the propagation paths of the wing cracks (anti-wing cracks) and shell-cracks that were observed inside of the relatively heterogeneous specimens ($m = 5.0$). When a pair of wing cracks (or anti-wing cracks) was observed to propagate toward the top and bottom of a specimen, the stress concentrations at the tips of the cracks increased and then were released behind the tips of the cracks. The wing cracks in the specimens with flaw dip angles of 45° and 60° changed their propagating directions from perpendicular to the flaw surface to parallel to the maximal compressive loading stress. The propagation of symmetric, shell-like cracks, which are a new type of crack in the 3D state (inside of the specimen) could be observed if the specimens with flaw dip angles of 30°, 45°, 60° and 75° were cut into two parts (Fig. 7b–e). These shell-like cracks initiated at the lateral part of the initial flaw at the same time as the wing cracks, and they propagated along the direction of the maximal compressive stress. No shell-like cracks were observed in the specimen with a flaw angle of 15° (Fig. 7a), and a fracture zone appeared around the inside contour of the flaw. Because the pre-existing flaw tended to be parallel to the applied compressive loading, there was not enough free space for tensile failure to occur at the inner edge of the flaw.

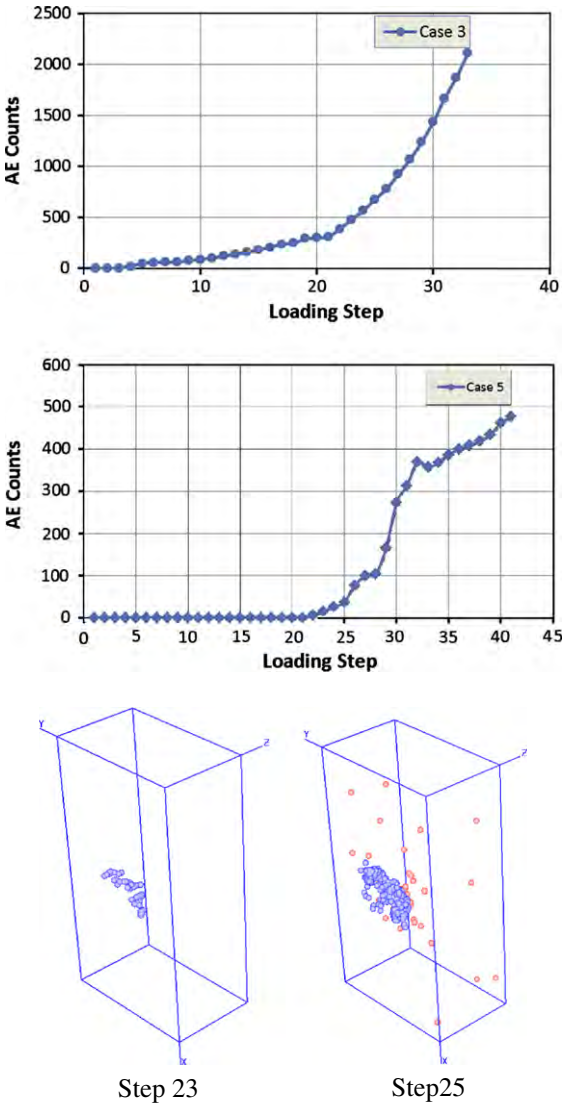

Fig. 6. Plot of acoustic emission counts in the early crack initiation stage for the specimen ($m = 5.0$) with dip angle of 45°.

In many studies, shell-like cracks have been regarded as extensions of wing crack. Based on our numerical results, wing cracks and shell-like cracks were observed to be attached to one another. Moreover, they propagated though different parts of the specimen and their growth behaviors were not the same; therefore, we refer to shell-like cracks as shell-like cracks in the 3D state so as to distinguish them from wing cracks in the 2D state.

Fig. 7a′–e′ depicts the results for the homogeneous specimen group ($m = 50$), wherein it can be observed that the flaw dip angle also influenced the propagation patterns of wing cracks and shell-like cracks. Shell-like cracks were observed in all of the specimen cross sections. The shell-like cracks propagated longer distances in the specimens with flaw dip angles of 45° and 60° in comparison to the other three specimens. In the specimens with flaw dip angles of 15° (Fig. 7a′) and 30° (Fig. 7b′), the shell-like cracks were observed to extend toward the back of the specimens, whereas, in the specimens with flaw dip angles of 45°, 60° and 75°, the crack propagation directions deviated from the maximal principal stress as a function of further loading (Fig. 7c′–e′), which caused the shell-like cracks to curl, as was observed by Dyskin et al. in their experimental studies [4,5].

Fig. 8 depicts the crack propagation patterns of the wing cracks and anti-wing cracks that appeared on the specimen surfaces when the load was increased to 90% of the peak load. According to Fig. 8, anti-wing cracks appeared in the more heterogeneous specimens ($m = 5$) with flaw dip angles of 45° and 60° (Fig. 8c–d). The anti-wing cracks were not observed in the crack initiation stage. Unlike the wing cracks, which were formed at the tips of the pre-existing flaws with dip angles of 15°, 30°, 45° and 60°, and the anti-wing cracks, which initiated at the tips of the pre-existing flaw with a dip angle of 75°, these anti-wing cracks appeared a certain distance from the pre-existing flaw instead of at the tips of the flaw. This phenomenon differs from the observations of the wing crack and anti-wing crack formations, which were observed to approximately symmetrically propagate along the maximal compressive stress, in that these anti-wing cracks did not symmetrically grow opposite to the direction of the propagation of the wing-cracks. As shown in Fig. 8c, the anti-wing crack on the left side of the specimen propagated both upward opposite to the wing crack and downward to the left tip of the pre-existing flaw. As for the specimen with the flaw dip angle of 60°, the anti-wing crack on the left side propagated downward and never joined the pre-existing flaw (Fig. 8d). It is a general consensus that compressive stress concentrates in the area where the anti-wing cracks appear. Guo et al. have observed anti-wing cracks in gabbro, and the growth of anti-wing cracks therein was observed to turn to the loading direction when the crack growth length equaled approximately half of the flaw length. They considered that the anti-wing cracks were induced by shear and compressive stresses [12].

The biggest difference between these two types of rock with different homogeneities was that no anti-wing cracks were observed for all five of the homogeneous specimens ($m = 50.0$). In addition, the cracks developed more smoothly and straight in this group. Many microfractures were observed along the propagating path in the more heterogeneous rocks ($m = 5$).

It was noted that the curling phenomenon of the wing cracks and shell cracks was observed in all of the specimens, regardless of flaw angle orientation or rock heterogeneity. For the specimens with flaw dip angles of 15°, 30° and 45°, the wing cracks changed

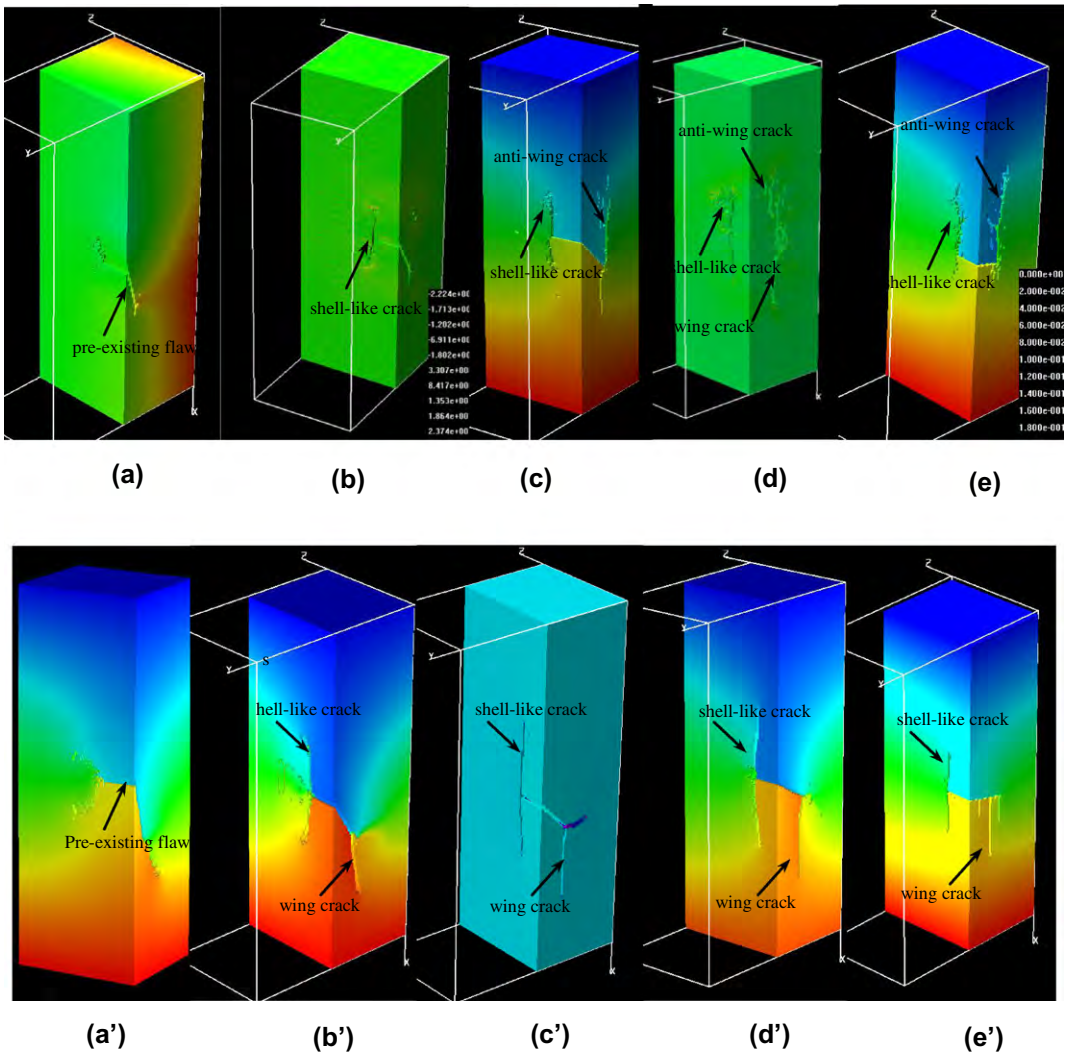

Fig. 7. The crack propagation patterns inside of the specimens with a pre-existing flaw with different dip angles (plan section B–B in Fig. 2). The first row (a–e) is for the relatively heterogeneous specimens (m = 5.0), and the second row (a′–e′) is for the relatively more homogeneous specimens (m = 50.0).

their propagation directions around the initial cracks without further elongation to parallel to the direction of the loading (Fig. 7(a–c and a′–c′). From the surface of the specimen, it could be observed that the wing crack propagation turned into the direction of the lateral boundary of the specimen. If we looked inside the specimens, the shell-like cracks therein would be observed to have curled either toward the front boundary or toward the back boundary of the specimen (Fig. 7). The wing cracks never propagated to the top or bottom boundaries under uniaxial compression. This phenomenon was also observed by Wong et al. [11] and Dyskin et al. [14] in their laboratory experiments. In the 2D state, wing cracks can reach the top and bottom boundaries without inside curling [5]. Curling under uniaxial compression distinguishes 2D from 3D fracture patterns.

To more clearly observe internal crack propagation, half of the specimen with the flaw dip angle of 45° was cut away to see the cross section of A′–A, as depicted in Fig. 3. Fig. 9a–c depicts the propagation process of the cracks inside of the specimen. When the wing cracks began to grow, the shell-like cracks began to propagate along the inside contour of the surface flaw close to the wing cracks (Fig. 9a). With further loading, the wing cracks and shell-like cracks continued to propagate, and the anti-wing cracks appeared at the surface of the specimen (Fig. 9b). As shown in Fig. 9c, a semi-ellipse on the cross section of A′–A was then formed due to the coalescence of the propagation of the anti-wing cracks and the shell-like cracks. On the other side of this specimen, the same fracture pattern can be found from the cross section near the other tip of the flaw (Fig. 9d). A new type of crack was observed to propagate perpendicular to the surface of the shell-like crack before the bursting failure of specimen (Figs. 9d and 10). When the wing cracks stopped propagating, this type of secondary crack began to initiate and then extended toward the back boundary of the specimen, resulting in an abrupt collapse of the specimen. These secondary cracks can be observed in the distribution of AE in Fig. 11c and b.

The AE technique was helpful to capture failure in the investigated rocks. Liu et al. [13] and Guo et al. [12] have conducted experimental investigations of 3D propagation processes in a type of surface fault using the AE technique. Fig. 11 depicts the AE distribution inside of the rock specimen that contained a flaw dip angle of 45° when the stress was increased to 82% of the peak strength. Fig. 11a–c depict a front side view, side view and top view of the specimen. The wing cracks and the shell-like cracks on each side of the prepared flaw coalesced together, and it is very difficult to make a distinction between these two types of cracks. It was obvious that the lengths of the wing cracks were longer than those of the shell-like cracks. Anti-wing cracks were observed on

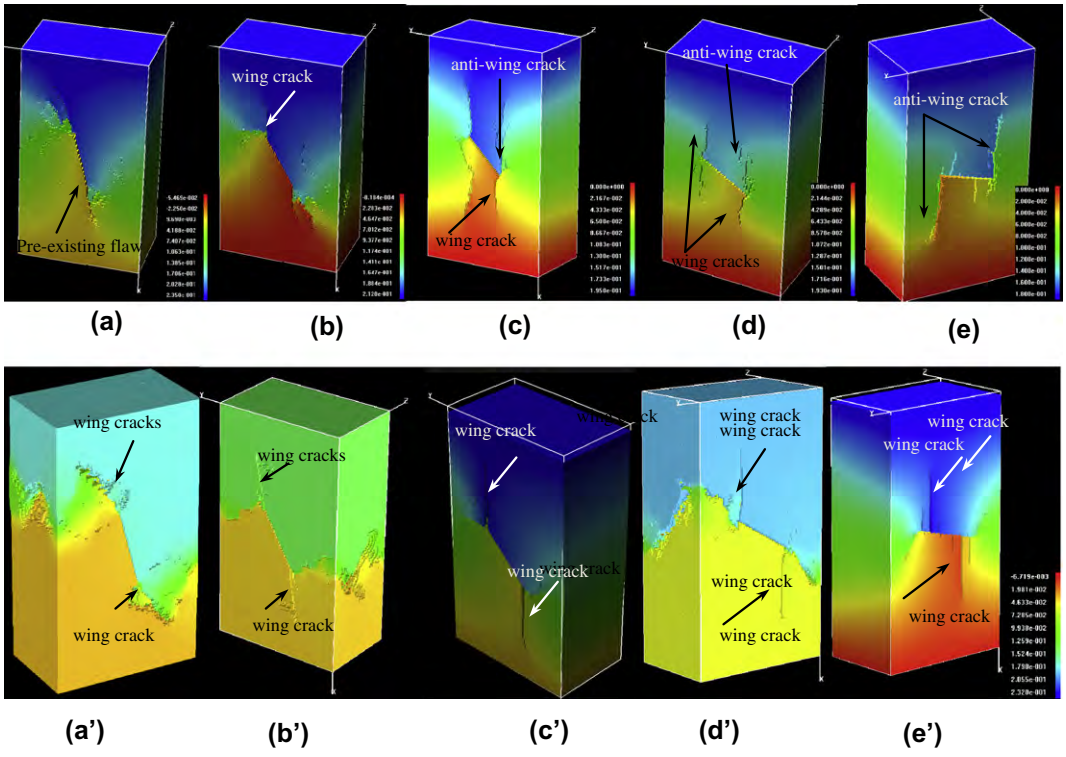

Fig. 8. Plot of the propagation of the wing cracks and anti-wing cracks on the surface of the specimens.

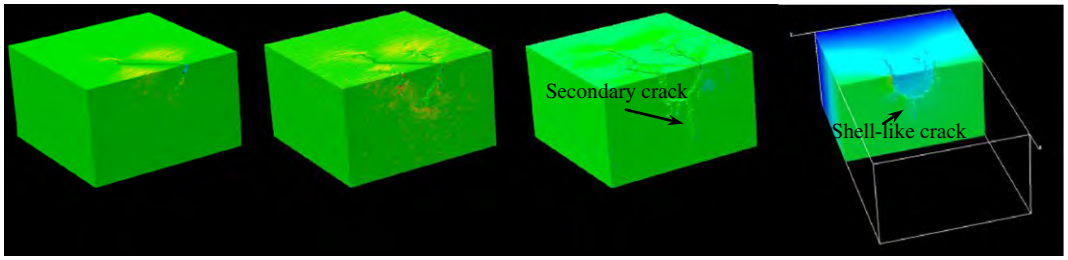

Fig. 9. Plot of propagation of the shell-like crack inside of the rock specimen that contains the flaw of 45° (m = 5.0). (a–c) show the fracture patterns in different loading step on section A–A. (d) shows the fracture pattern on the section C–C.

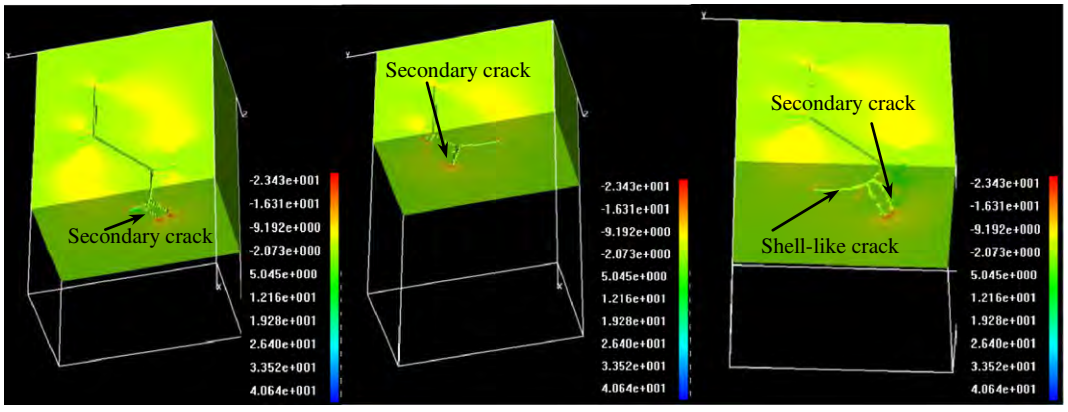

Fig. 10. Crack propagation inside of the specimen with the dip angle of 45° for the pre-existing flaw (m = 50.0).

the left bottom and right top corners of the specimen. If the specimen were viewed from the top, all of the observed AE points form a complete semi-ellipse that is similar to a cylindrical shell (Fig. 11c).

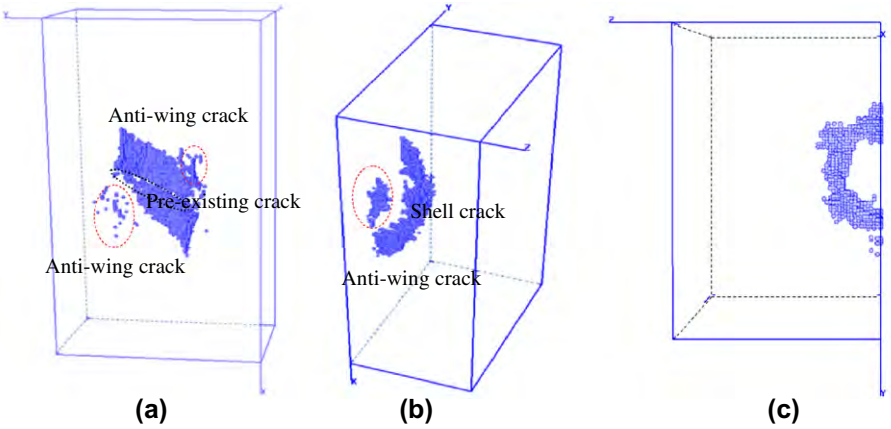

Fig. 11. Plot of the acoustic emission distribution inside of the rock specimen with the flaw dip angle of 45° (m = 5.0).

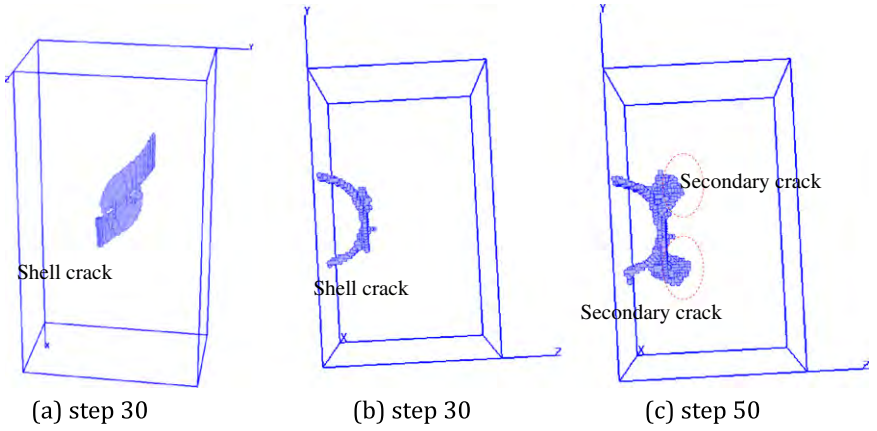

Fig. 12. Plots of the acoustic emission distribution inside the rock specimen with the flaw dip angle of 45° (m = 50.0).

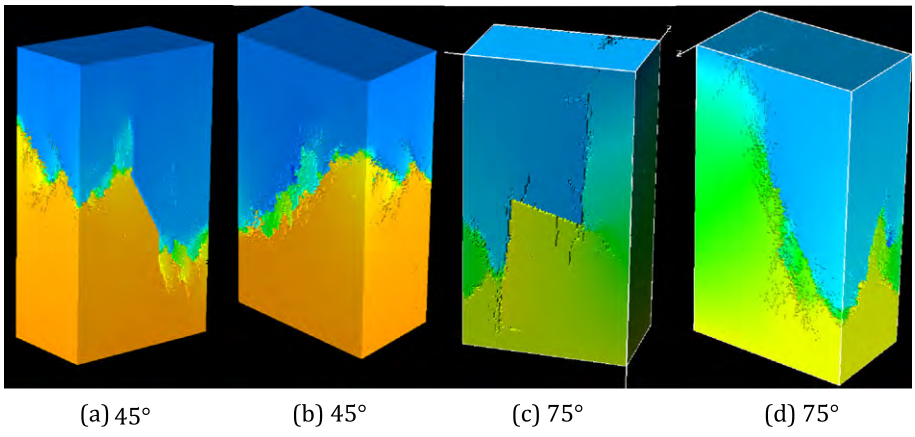

Fig. 13. Final fracture patterns for the homogeneous specimens. (a) and (c) are front view, and (b) and (d) are back view.

Fig. 12 depicts the AE distribution for the relatively homogeneous specimen with the flaw dip angle of 45°. As mentioned above, for anti-wing cracks, AEs were not observed in the more homogeneous rock specimen. The crack surface in the homogeneous specimen was relatively smooth, and the observed AE events gathered along the crack propagation path. In Fig. 11c, AEs corresponding to the secondary crack of the shell-like cracks can be observed at step 50 before the failure of the specimen. It can be predicted that if a specimen that contains a full elliptic inner flaw is uniaxially compressed, then the prepared flaw will be surrounded by an entire shell-like crack on both the upper and lower surfaces.

4.3. Failure stage of the specimens

With increasing uniaxial loading, the specimens exhibited bursting failure at the peak stress, wherein the wing cracks, shell-like cracks and secondary cracks extended to the back of

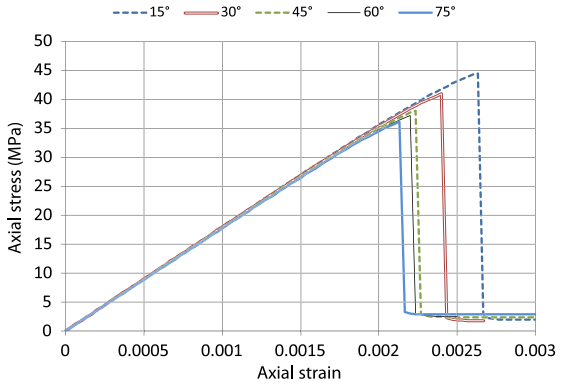

(a) m=5.0

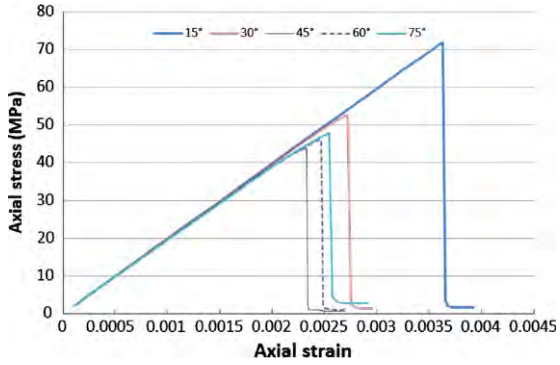

(b) m=50.0

Fig. 14. Complete axial stress–strain curves for the specimens.

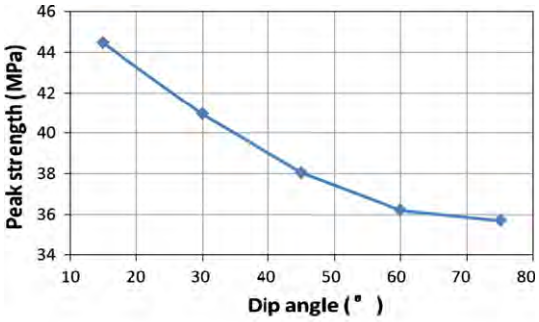

(a) m=5.0

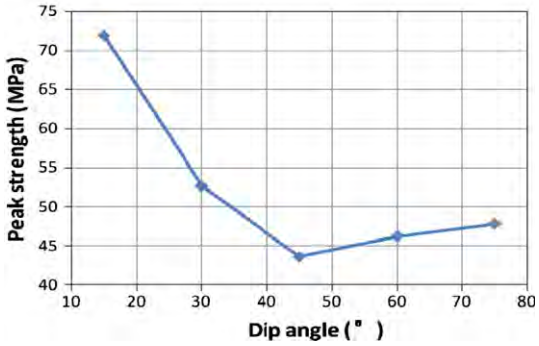

(b) m=50.0

Fig. 15. Plots of the peak strength of the heterogeneous specimens versus the flaw dip angle.

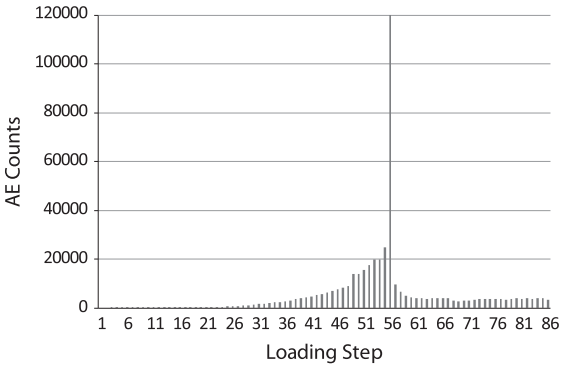

Fig. 16. The acoustic emission counts in each step for the specimen with the flaw dip angle of 45°.

the specimen. Meanwhile, many new tensile fractures appeared near the wing cracks (or anti-wing cracks). These tensile fractures ran to the lateral boundary of the specimen. The specimens that contained flaws with a dip angle of 45° were divided into two parts in a shear failure mode (Fig. 13a and b). As for the specimen that contained a flaw with a dip angle of 75°, macroshear fractures were also observed on the back of this specimen due to the propagation of the shell-like cracks inside (Fig. 13c–d).

Complete axial stress–strain curves were obtained via the numerical model, as shown in Fig. 14. Almost all of the specimens in these two groups underwent the same elastic deformations before the propagation of cracks. The specimens exhibited brittle failure at the peak strength. As indicated in Fig. 15a, following an increase in the flaw dip angle, the peak strengths for the specimens in the heterogeneous group gradually decreased. For the relatively homogeneous specimens, the peak strength decreased when the flaw dip angle increased from 15° to 45° but increased when the dip angle increased from 45° to 75° (Fig. 15b).

Abrupt specimen failure complicated the capture of any failure signals before collapse. Fig. 16 depicts the AE counts in each step for the specimen with the flaw dip angle of 45°. Therein, three increases in the AE rate in the loading process can be observed, indicating the initiation, propagation and coalescence of cracks in the specimen. The bursting fracture at the peak point made it difficult to predict the final failure in advance.

5. Discussions

Based on the above numerical results, the complicated surface flaw initiation and propagation behaviors are discussed in detail below:

5.1. Heterogeneity has a significant influence on the fracture of 3D surface flaws

Three aspects about the influence of the rock heterogeneity will be discussed: the crack propagation path, anti-wing cracks, and the peak strength.

First, the propagation path in rocks depends not only on the stress state but also on the heterogeneity of the rock. Cracks will propagate toward the weak zone where stress concentrates, such that the direction of crack propagation will be more likely to change in heterogeneous rocks that are even subjected to uniaxial compression; however, in relatively homogeneous rocks, the mechanical parameters throughout the entire specimen are uniform, so the direction of crack propagation will only be determined by the stress state. As shown in Fig. 7, the crack propagation path in the specimens with the higher homogeneity index ($m = 50$) was

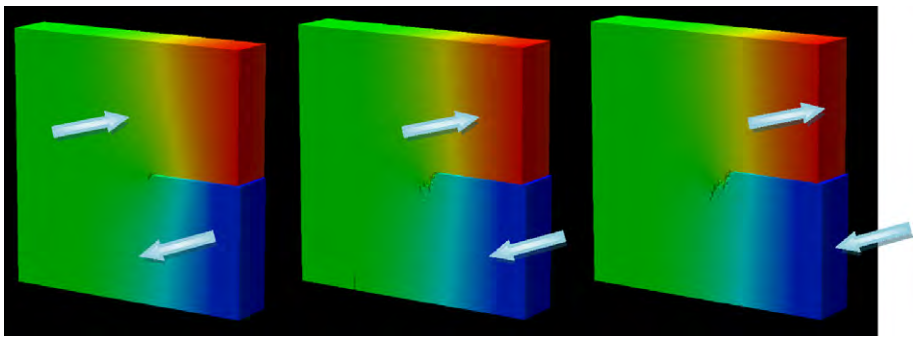

Fig. 17. Fracture pattern in the numerical specimen (m = 5.0) containing a pre-existing flaw under anti-plane loading.

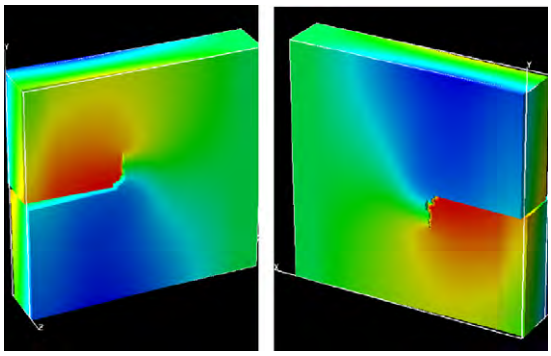

Fig. 18. Fracture pattern in the numerical specimen (m = 50.0) containing a pre-existing flaw under anti-plane loading.

smoother and straighter. Moreover, both the wing cracks and the shell-like cracks propagated a longer distance in this homogeneous group. Second, the peak strength for the relatively homogeneous specimens was much higher than that for the heterogeneous group. Even though only two groups were considered in the present paper, the difference in the peak strength between these two types of rocks was remarkable (Fig. 14). Third, anti-wing cracks did not appear in the relatively higher homogeneous specimens. In the first group, anti-wing cracks initiated in the specimens with flaw dip angles of 45° and 60° before the final failures of the specimens, and a pair of anti-wing cracks even appeared at the beginning of the propagation stage. No anti-wing cracks were observed in all of the specimens that had a higher homogeneity index (m = 50.0) (Fig. 7) before final failure. These data indicate that the materials used in experiments concerning the 3D crack investigation of heterogeneous rocks cannot be replaced by some homogeneous materials, such as resin or glass. In experimental studies, petal-like cracks were often observed near the contours of the prepared flaws. This type of crack seems to be a shell-like crack that results from heterogeneity in the specimens and a discrepancy in flaw preparation. In addition, the friction between the loading platen and the end of the specimen in experimental investigations will also influence subsequent crack initiation and propagation [2,3].

5.2. The dip angle between the maximal principal stress and the surface of a pre-existing flaw affects the crack propagation pattern as well as the mechanical behavior of the specimen

The flaw dip angle affects the appearance of the wing cracks. No wing cracks were observed in the specimen with a flaw dip angle of 75°. When the dip angle was greater than 30°, anti-wing crack appeared in the heterogeneous rocks. A large dip angle contributes to the propagation of shell-like cracks. In addition, the appearance of anti-wing cracks influenced the peak strengths of the specimens. The peak strength gradually decreased with increasing dip angle to the maximal principal stress in the relatively heterogeneous rock specimens, whereas, in the homogeneous group, the peak strength decreased when the dip angle varied from 15° to 45° but increased when the angle increased from 45° to 75° (Figs. 14 and 15).

The experimental data obtained by Wong et al. showed that the stress decreased gradually when the dip angle of the flaws

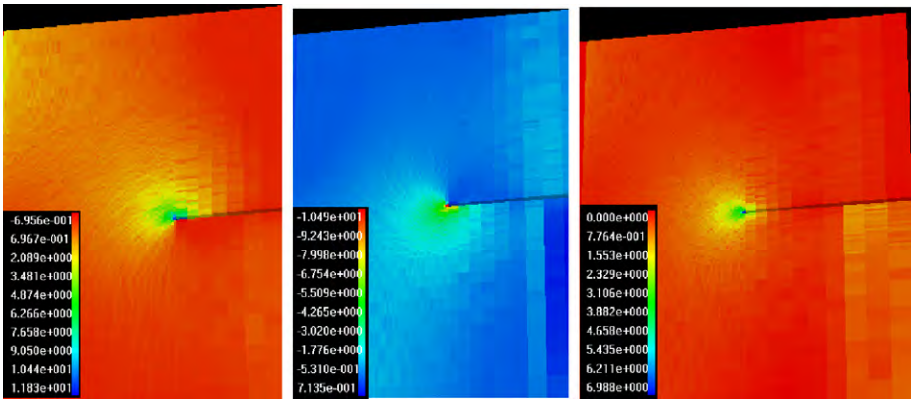

(a) Maximal pinrcipal stress (b) Minimal pincipal stress (c) Maximal shear stress

Fig. 19. The stress concentration around the tip of the pre-existing flaw.

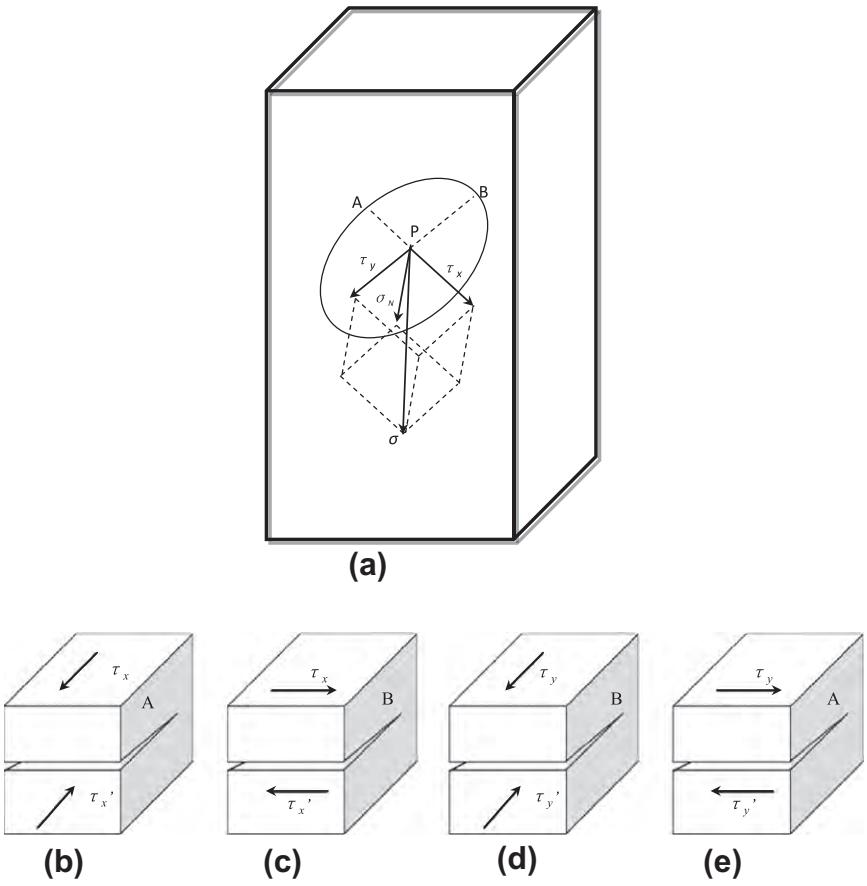

Fig. 20. Plots of the stress state of the surface flaw in the model subjected to uniaxial compression.

increased from 30°, 45°, 60° to 75° in gabbro [12]. Figs. 14a and 15a agreed with their results.

The homogeneous specimens followed this decrease–increase rule because their strengths were exclusively determined by the initiation and propagation of the wing cracks and shell-like cracks; however, when the dip angle of the pre-existing flaw was greater than 45°, the strengths of the relatively heterogeneous specimens mainly depended on the anti-wing cracks, which played a dominant role in specimen failure. The fracture mode was completely changed by the occurrence of anti-wing cracks, leading to a gradual reduction in strength when the dip angle increased from 45° to 75°. The same increasing–decreasing phenomenon has widely been observed in rocks that contain through joints with different orientations [43]. The fracturing of rock specimens that contain through joints can be regarded as 2D problems, in which the anti-wing could not be observed [34].

5.3. Is shell-like crack or petal-shape crack a type of Mode III crack?

Adams and Sines [16] performed investigations of the mechanism of 3D crack growth in uniaxial compression, and they have indicated that petal-shape crack is a type of Mode III crack in their studies. To understand this fracture mechanism, a pure anti-plane loading test was numerically simulated (Fig. 17). A flaw was prepared to penetrate the numerical specimen with the homogeneity index of $m = 5.0$ at one end. The other end of the specimen was fixed. A pair of stresses, in the contrary direction and perpendicular to the surfaces of the numerical specimen, was applied on the upper right end and the lower right end of the sample to implement anti-plane shear fracture.

Fig. 17 depicts the fracture process of the numerical specimen under Mode III loading. The crack was observed to initiate at the tip of the flaw, wherein elemental damage was found; however, the newly formed crack did not propagate along the direction of the pre-existing flaw, as predicted by Mode III fracturing. The crack extended to the bottom of the specimen at a dip angle of 45°. The conditions of the numerical test strictly complied with Mode III fracturing; however, no Mode III cracks occurred. Another numerical test was undertaken in the more homogeneous rocks. A specimen with a homogeneity index of 50 (representing a homogenous rock) was subjected the same boundary conditions. As shown in Fig. 18, the crack propagated perpendicular to the surface of the prepared flaw.

It seems that anti-plane shear loading will not cause Mode III crack. Due to the fact that the rocks have higher compressive strengths (shear strength) but much lower tensile strengths, Mode III type fractures will never occur under anti-plane loading. The distribution of the maximal principal, minimal principal and maximal principal shear stresses near the tip of the flaw on the front surface is shown in Fig. 19. A strong compressive stress can be observed to be concentrated on the upper right side of the tip, a strong tensile stress can be observed to be concentrated on the lower right side, and a strong shear stress can be observed to be concentrated on the front of the tip. The crack potentially propagates either along the surface of the prepared flaw in shear failure mode or propagates toward the lower right direction in the tensile failure mode. Rocks are typically brittle materials, having much higher shear strengths than tensile strengths. Tensile fracture may more likely occur under anti-plane loading. In the numerical simulation of surface flaws, shell-like cracks propagated along the direction perpendicular to the pre-existing flaw. This is the reason why the actual lateral growth of the initial crack in its own plane was not observed in the experiments of Adams and Sines [16] and Cannon et al. [17] on PMMA blocks with semi-circular cracks.

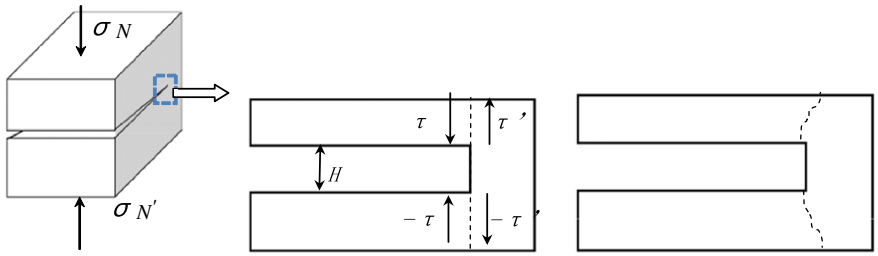

Fig. 21. Potential Mode II fracture in the crack model with a specified thickness subjected to compression.

Because anti-plane loading will not necessarily lead to Mode III crack in rocks, many researchers have performed compression-shear tests or torsion tests to obtain Mode III crack when they failed to obtain Mode III crack in anti-plane shear tests [44–46]. In the compression-shear test, the tensile stress at the tip of the pre-existing flaw was constrained due to the applied strong compressive stress. The shear fracture of Mode III crack might be easier to induce than Mode I crack; however, this is another important issue that warrants more discussion.

5.4. The fracture mechanism of 3D crack is difficult to understand due to the complex stress state around it during the specimen failure process

Fig. 20a depicts a model that contains a prepared 3D elliptic through flaw that has been subjected to uniaxial compression. If we establish a local coordinate system above the pre-existing flaw, the vertical compressive stress that acts on the crack can be divided into three components: the shear stress τ_x and τ_y and the normal stress σ_N. These three components have different effects on the initiation and propagation of cracks at different points around the edge of the pre-existing flaw. The shear stress τ_x will cause Mode II crack at point A located at the tip of the major axis of the elliptic flaw (Fig. 20b), whereas, τ_x will perform anti-plane loading at point B, which is located at the tip of the minor axis (Fig. 20c). Similarly, the shear stress τ_y will cause anti-plan loading at point A (Fig. 20d), whereas, τ_y will perform Mode II cracking at point B (Fig. 20e). From the numerical results, we can only find Mode II crack in the specimens with a flaw dip angle of 15° before they suffer bursting failure. These data imply that anti-plane loading (Mode III-type loading) leads to the initiation and propagation of shell-like cracks.

Because of the complex stress state around the edge of a 3D flaw, shell-like cracks may actually be a kind of mixed-mode crack. In traditional fracture mechanics, there is an assumption that a flaw (or crack) has no thickness; however, the thicknesses of flaws and joints in rocks may range from several centimeters to many meters, and, moreover, faults in the Earth's crust have thicknesses on the order of several kilometers. The thicknesses of 3D flaws should not be ignored in fracture mechanics. Shear stresses exist along all of the walls of a flaw due to the normal stress applied over the flaw if it has any thickness (Fig. 21). This type of shear stress will result in Mode II crack that is parallel to the wall of the flaw, and it also contributes to the initiation and propagation of shell-like cracks, which extend perpendicular to the pre-existing flaw. In general, shell-like crack may be induced by mixed-mode loading.

6. Conclusions

Using RFPA^{3D}, this paper has investigated the influences of rock heterogeneity and pre-existing flaw dip angle on 3D crack initiation and propagation. The initiation and propagation of surface flaws are affected by many factors, such as flaw orientation, flaw thickness, flaw depth, and loading style. The present numerical simulation only focused on the orientation of the prepared flaw and heterogeneity in the rock specimen. Although the role of these parameters needs further experimental and theoretical analysis, and the propagation processes of 3D cracks under complex loading styles should be further investigated, the numerical results of this study demonstrate many phenomena that have already been shown in laboratory experiments; however, many of these fracture phenomena results direct the necessity of additional experiments. This study highlights some interesting phenomena for improving the understanding of the mechanism of 3D rock fracturing. Some of the key results are summarized below:

(1) The initiation and propagation processes wing cracks, anti-wing cracks and shell-like cracks that were subjected to uniaxial compression were numerically simulated by RFPA^{3D}.
(2) Crack propagation in homogeneous materials differs from that in heterogeneous, rock-like materials. Anti-wing crack cannot be observed in homogeneous materials. The failure pattern for relatively homogeneous specimens does not resemble that of heterogeneous rock specimens. PMMA and glass-like materials should not be used to study the fracture of rock-like materials in laboratory experiments.
(3) Wing crack on the surface and shell-like crack inside of the specimens cannot propagate to the top or bottom of specimens due to the curling of these two types of cracks toward the lateral boundary when they extend to a certain distance.
(4) The dip angle between the maximal principal stress and the surface of the surface flaw affects the occurrence of wing cracks (wing cracks) and the peak strength of the specimen.
(5) The numerically simulated results indicate that Mode III loading (anti-plane loading) does not lead to Mode III fracture in rocks due to their high ratios of compressive strength to tensile strength. This finding can help explain why the lateral growth of an existing flaw in its own plane has not been observed in laboratory experiments.

Acknowledgements

This work was supported by National Program on Key Basic Research Project of China (973 Program) (Grant No. 2011CB013500), the National Natural Science Foundation of China (Grant Nos. 51121005, 51079017, 50820125405 and 51004020), the Foundation for the Author of National Excellent Doctoral Dissertation of PR China (No.200960) and the Program for New Century Excellent Talents in University (NECT-09-0258). The work was partially supported by ARC CoE Early Career Award Grant CE110001009, for which the authors are very grateful.

References

[1] Paul B. Macroscopic criteria for plastic flow and brittle fracture. In: Liebowitz H, editor. Fracture and advanced treatise, vol. II; 1968. p. 313–496.

[2] Peng S, Johnson AM. Crack growth and faulting in cylindrical specimens of Chelmsford granite. Int J Rock Mech Min Sci Geomech Abstr 1972;9:37–86.
[3] Wong RHC, Law CM, Chau KT. Crack propagation from 3-D surface fractures in PMMA and marble specimens under uniaxial compression. Int J Rock Mech Min Sci 2004;41(3):360–6.
[4] Dyskin AV, Sahouryeh E, Jewell RJ. Influence of shape and locations of initial 3D cracks on their growth in uniaxial compression. Eng Fract Mech 2003;70(15):2115–36.
[5] Dyskin AV, Germanovich LN, Jewell RJ, Joer H, Krasinski JS, Lee KK. Study of 3-d mechanisms of crack growth and interaction in uniaxial compression. ISRM News J 1994;2(1):17–20.
[6] Teng CK, Yin XC, Li SY. An experimental investigation on 3D fractures of non-penetrating crack in plane samples. Acta Geophys Sin 1987;30(4):371–8. in Chinese.
[7] Yin XC, Li SY, Li H. Experimental study of interaction be-tween two flanks of closed crack. Acta Geophys Sin 1988;31(3):307–14. in Chinese.
[8] Sahouryeh E, Dyskin AV, Germanovich LN. Crack growth under biaxial compression. Eng Fract Mech 2002;69(18):2187–98.
[9] Wong RHC, Huang ML, Jiao MR. The mechanisms of crack propagation from surface 3-D fracture under uniaxial compression. Key Eng Mater 2004;261:219–24.
[10] Wong RHC, Guo YS, Li LY. Anti-wing crack growth from surface fault in real rock under uniaxial compression. In: Gdoutos EE, editor. The 16th European conference of fracture (ECF16), 2006, July 3–7, Alexandropoulos, Greece. Amsterdam: Springer; 2008. p. 825–6.
[11] Wong RHC, Guo YS, Chau KT. The fracture mechanism of 3D surface fault with strain and acoustic emission measurement under axial compression. Key Eng Mater 2007;358:2360–3587.
[12] Guo YS, Wong RHC, Zhu WS. Study on fracture pattern of open surface-flaw in gabbro. Chinese J Rock Mech Eng 2007;26(3):525–31.
[13] Liu LQ, Liu PX, Wong HC, Ma SP, Guo YS. Experimental investigation of three-dimensional propagation process from surface fault. Sci China Ser D: Earth Sci 2008;51(10):1426–35.
[14] Dyskin AV, Jewell RJ, Joer H, Sahouryeh E, Ustinov KB. Experiments on 3-d crack growth in uniaxial compression. Int J Fract 1994;65:77–83.
[15] Knauss WG. An observation of crack propagation in anti-plane shear. Int J Fract 1970;6(2):183–5.
[16] Adams M, Sines G. Crack extension from flaws in a brittle material subjected to compression. Tectonophysics 1978;49:97–118.
[17] Cannon NP, Schulson EM, Smith TR, Frost HJ. Wing cracks and brittle compressive fracture. Acta Metall Mater 1990;38(10):1955–62.
[18] Chen CS, Pan E, Amadei B. Fracture mechanics analysis of cracked discs of anisotropic rock using the boundary element method. Int J Rock Mech Min Sci 1998;35(2):195–218.
[19] Shen B, Stephansson O. Numerical analysis of mixed mode I and mode II fracture propagation. Int J Rock Mech Min Sci Geomech Abst 1993;30(7):861–7.
[20] Shen B. The mechanism of fracture coalescence in compression – experimental study and numerical simulation. Eng Fract Mech 1995;51(1):73–85.
[21] Feng XT, Pan PZ, Zhou H. Simulation of the rock microfracturing process under uniaxial compression using an elasto-plastic cellular automaton. Int J Rock Mech Min Sci 2006;43(7):1091–108.
[22] Pan PZ, Feng XT, Hudson JA. Study of failure and scale effects in rocks under uniaxial compression using 3D cellular automata. Int J Rock Mech Min Sci 2009;46(4):674–85.
[23] Rozycki P, Moes N, Bechet E, Dubois C. X-FEM explicit dynamics for constant strain elements to alleviate mesh constraints on internal or external boundaries. Comput Method Appl Mech Eng 2008;197(5):349–63.
[24] Gregoire D, Maigre H, Rethore J, Combescure. Dynamic crack propagation under mixed-mode loading – comparison between experiments and X-FEM simulations. Int J Solid Struct 2007;44(20):6517–34.
[25] Colombo D, Massin P. Fast and robust level set update for 3D non-planar X-FEM crack propagation modeling. Comput Method Appl Mech Eng 2011;200(25–28):2160–80.
[26] Tang CA, Lin P, Chau KT, Wong RHC. Analysis of crack coalescence in rock-like materials containing three flaws—Part II: numerical approach. Int J Rock Mech Min Sci 2001;38(7):925–39.
[27] Liang ZZ, Tang CA, Zhang YB. 3-D micromechanics model for progressive failure analysis of laminated cylindrical composite shell. Key Eng Mater 2005;297–300:1113–9.
[28] Liang ZZ, Tang CA, Li HX, Zhang YB. Numerical simulation of the 3D failure process in heterogeneous rocks. Int J Rock Mech Min Sci 2003;41(3):419.
[29] Tang CA, Zhang YB, Liang ZZ, Xu T, Tham LG, Lindqvist PA, et al. Fracture spacing in layered materials and pattern transition from parallel to polygonal fractures. Phys Rev E 2006;73(5):056120.
[30] Wang SY, Lam KC, Au SK, Tang CA, Zhu WC, Yang TH. Analytical and numerical study on the pillar rockbursts mechanism. Rock Mech Rock Eng 2006;39(5):445–67.
[31] Wang SY, Sloan SW, Huang ML, Tang CA. Numerical study of failure mechanism of serial and parallel rock pillars. Rock Mech Rock Eng 2010;44:179–98.
[32] Wang SY, Sun L, Au ASK, Yang TH, Tang CA. 2D-numerical analysis of hydraulic fracturing in heterogeneous geo-materials. Constr Build Mater 2009;23(6):2196–206.
[33] Wang SY, Sloan SW, Sheng DC, Tang CA. Numerical analysis of the failure process around a circular opening in rock. Comput Geotech 2012;39:8–16.
[34] Wong RHC, Chau KT, Tang CA. Analysis of crack coalescence in rock-like materials containing three flaws—Part I: experimental approach. Int J Rock Mech Min Sci 2001;38(7):909–24.
[35] Atkinson BK. Fracture mechanics of rock. Beijing: Seismological Press; 1992. Translated by Yin XC.
[36] Weibull W. A statistical theory of the strength of materials. Ing Vet Ak Handl 1939;151:5–44.
[37] Tang CA. Numerical simulation of progressive rock failure and associated seismicity. Int J Rock Mech Min Sci 1997;34:249–61.
[38] Tang CA. A new approach to numerical method of modelling geological processes and rock engineering problems. Eng Geol 1998;49:207–14.
[39] Handin J, Heard HC, Magouirk JN. Effect of the intermediate principal stress on the failure of limestone, dolomite and glass at different temperatures and strain rates. J Geophys Res 1967;72:611–40.
[40] Mogi K. Effect of intermediate principal stress on rock failure. J Geophys Res 1967;72:5117–31.
[41] Michelis P. True triaxial cyclic behavior of concrete and rock in compression. Int J Plast 1987;3(2):249–70.
[42] Yu MH. Unified strength theory and its applications. Berlin: Springer-Verlag; 2004.
[43] John AH, John PH. Engineering rock mechanics—Part I: an introduction to the principles. Elsevier Science; 2000.
[44] Xie HF, Rao QH, Wang Z. Fracture morphology analysis of brittle rock under anti-plane shear (mode III) loading. Chin J Rock Mech Eng 2007;26(9):1832–9.
[45] Farshada M, Flüelera P. Investigation of mode III fracture toughness using an anti-elastic plate bending method. Eng Fract Mech 1998;60(5/6):597–603.
[46] Li LY, Ning HL, Xu FG. Test and numerical analysis of fracture toughness model III fracture. Chin J Rock Mech Eng 2006;25(12):2523–8.